Latent Cure Epoxy Resins for Reliable Joints in Secondary-Bonded Composite Structures

Frank L. Palmieri[1]*, Tyler B. Hudson[1], Austin J. Smith[1], Roberto J. Cano[1], Jin Ho Kang[2], Yi Lin[2], Lauren J. Abbott[3], Bryson Clifford[4], Isaac J. Barnett[4], and John W. Connell[1]

[1]NASA Langley Research Center, Hampton, VA, 23681, USA

[2]National Institute of Aerospace, Hampton, VA, 23666, USA

[3]NASA Ames Research Center, Moffett Field, CA, 94035, USA

[4]NASA Internships Fellowships and Scholarships Program, Hampton, VA, 23681, USA

*Corresponding Author: frank.l.palmieri@nasa.gov

ABSTRACT

In high-performance polymer matrix composite assemblies, adhesive bonding is generally superior to mechanical fastening in structural performance and manufacturing efficiency. However, adhesive bonds are susceptible to minute levels of contamination accumulated during assembly that can lead to unpredictable, weak bonds. Current methods of measuring bond strength are all destructive mechanical tests. To overcome these challenges, redundant load paths (e.g., mechanical fasteners) are often implemented in secondary-bonded, primary-structures, which can greatly reduce structural performance. This study investigated reformulated aerospace epoxy matrix resins with stoichiometric

offset to inhibit cure of the matrix resin prior to assembly. Inhibited resins can reflow and mix across the joint interface, which eliminates the material discontinuity and forms a homogenous joint with reliable fracture properties. The goal of this study was to develop and demonstrate secondary composite assemblies that are mechanically and microscopically indistinguishable from a co-cured composite joint. This article describes the development of latent epoxy resins, the fabrication of test articles, and the mechanical properties measured from experimental joints compared with conventional, co-cured laminates. Methods of in-line quality control using and infrared spectroscopy and post-assembly forensics are also described. The final mode-II fracture toughness measured from precracked AERoBOND specimens was similar to that measured from co-cured laminates indicating that later cure epoxy materials could be a suitable replacement for secondary bonding.

Keywords: A. Polymer-matrix composites (PMCs), B. Cure behavior, E. Assembly, Redundant fasteners

1. INTRODUCTION

Polymer matrix composites are used in high performance aerospace structures because of their excellent specific strength, toughness, and stiffness along the fiber direction. To realize the full performance advantages of composites, complex, built-up structures must be assembled using adhesives; however, adhesive bonds are susceptible to minute levels of contamination accumulated during manufacturing that can lead to unpredictable, weak bonds. Additionally, there are no non-destructive techniques to measure bond strength. For these reasons, regulating organizations such as the Federal Aviation Administration (FAA)

often require redundant load paths to achieve certification for civil transport aircraft. Manufactures commonly install tens of thousands of redundant fasteners in composite airframes to ensure safety in critical applications but also adding tremendous complexity, time, and cost, while significantly reducing performance of the airframe [1-4]. The inherent uncertainty in adhesive bonds stems from the material discontinuity at the composite-to-adhesive interfaces, which are susceptible to contamination [5-7]. In contrast, co-cured composites, although limited in size and complexity, result in predictable structures that are certifiable for commercial aviation with reduced dependence on redundant load paths [1, 8]. Under NASA's Convergent Aeronautics Solutions (CAS) Project, the Adhesive Free Bonding of Composites (AERoBOND) project developed and tested a novel means of assembly using off-stoichiometric epoxy resin systems to produce a latent cure effect. The objective of the AERoBOND project was to demonstrate a method to achieve co-cure joint performance using a secondary-bonding manufacturing process. The success of the process was judged by mechanical performance, optical inspection of the interface to visually verify the co-cured appearance of the joint, and infrared spectroscopy to observe the chemical homogeneity and cure state.

1.1 Latent Polymerization in Epoxies

The single-component (1K) epoxy formulations commonly used in high performance structures such as airframes are formulated for a latent cure at elevated temperature to extend shelf life and working time (out time) at room temperature. The cure latency in state-of-the-art resins comes from crystalline hardeners such as dicyandiamide or diaminodiphenyl sulfone that melt at elevated temperature (>170 °C) [9]. More recently, resin systems have

been developed with improved out-time while simultaneously reducing the cure temperature of the resin. Recently, Zhang, et al., showed that epoxies hardened with a combination of imidazole and halogenated derivatives of bisphenol A exhibited five months of shelf life while curing effectively at temperatures less than 100 °C [10]. Wang, et al., studied mixtures of benzoxazines and amines in equilibrium to affect cure latency. These components react and form a stable equilibrium with an intermediate polymer [11]. The irreversible, crosslinked polymer network formed upon heating over 120 °C.

The AERoBOND process requires that the bulk of the part reach its full cure state, while the faying surface remain latent. In airframe manufacturing, latent epoxies with cure temperature near 180 °C are standard in primary composite structures, so thermal cure latency is not effective to prevent the fay surfaces from curing. A different latency mechanism is needed to suppress curing at the faying surfaces until the parts are assembled. To achieve this latency, three options are possible: 1) cool the faying surface to prevent the material from reaching the cure temperature, 2) chemically block the reactive sites of the monomers to prevent polymerization until unblocked, 3) offset the stoichiometry of the resin such that polymerization stops when the limiting reagent is consumed. The option to cool the faying surfaces would require specialized tooling and instruments to be implemented in an autoclave at great cost and complexity. Hydrolytically labile imines were investigated as blocked hardeners for epoxy resins with some success, but the use of water and catalyst for deprotection was slow and lead to concerns about porosity in the cured composite [12]. Offset stoichiometry suppresses cure by limiting one of the components in a two-component system and then using passive mass transfer to diffuse the limiting reagent into the faying

surface after assembly. This technique can be applied to current commercial resin systems and is applicable to multiple two-component resin systems without adding new catalysts or modifying cure chemistries. MacAdams et al., patented offset epoxy resins to prepare surfaces for bonding. A small stoichiometric offset is used to prevent full cure of matrix resin at the faying surface and promotes covalent bonding at the faying surface with adhesives after assembly [13]. AERoBOND technology is similar but uses larger stoichiometric offset and retains mobility in the faying surface resin even after primary cure to allow for mass transfer and equalization of the resin stoichiometry.

1.2 Example Assembly Process

The proposed technology uses a stoichiometric offset of the hardener-to-epoxy ratio on the faying surfaces of laminates. Insufficient hardener in resin formulation prevents complete cure the of the resin formulation during an epoxy cure cycle up to 177 °C. Assembly of the partially cured components in a subsequent "secondary-co-cure" process results in a joint with no material discontinuities (Figure 1).

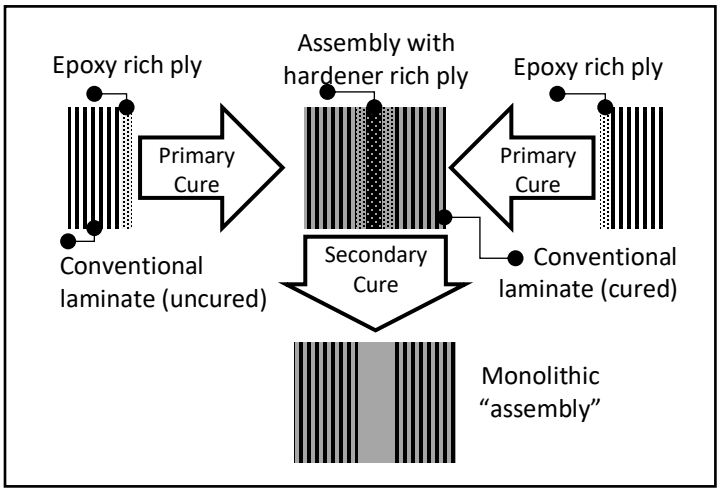

Figure 1. Schematic of assembly process using offset resin and reinforcing fiber.

In one embodiment of this technique, composite components are prepared with surfaces that are stoichiometrically rich with epoxy functional groups (Figure 1). During the primary cure, the epoxy rich (ER) resin mixes with the conventional resin (CR), but the offset stoichiometry in the ER surfaces limits the advancement of molecular weight, and the resin on the faying surfaces remains flowable at elevated temperature with intact reactive groups even after the primary cure. In step 2, the composite panels are assembled with a ply of hardener rich (HR) material between the ER surfaces. During secondary cure, the ER and HR plies intermix and cure to form a composite assembly with no discernable interface, analogous to a conventional, co-cured laminate. During the primary and secondary cure cycles, increased temperature reduces the viscosity of the uncured resin allowing flow, intermixing, interdiffusion, and consolidation. During the secondary cure step, intermixing of the HR and ER resins occurs, which eliminates material discontinuity at the joint interface. By combining the HR and ER resins, stoichiometric equivalence is achieved, and the molecular weight of the resin can advance until vitrification occurs.

1.3 Material and Process Parameters

The successful fabrication of an HR/ER joint depends on multiple, interdependent material and process parameters including epoxy precursor characteristics, stoichiometric offset, initial degree of cure, fiber volume fraction, ply thickness, residual solvent, number of plies, cure cycle temperature profile, and bagging scheme. Previous work using rheology and calorimetry [14, 15] indicated that an ER r-value ≤ 0.15 prevented gelation during primary cure where r is defined in equation 1 as:

Equation 1: $$r = \frac{eq_H}{eq_E} \equiv \frac{molar\ equivalents\ of\ hardener}{molar\ equivalents\ of\ epoxy}$$

In conventional aerospace epoxy resin formulations, the *r*-value is typically ~0.8 in order to optimize mechanical properties of the cured polymer [16]. For this study, the *r*-value of the HR resin was ≥ 2.5 in order to increase the homogenized stoichiometry of the AERoBOND joint. The mass balance in Eq. 2 and Eq. 3 was used to calculate the theoretical *r*-value obtained after secondary cure assuming complete mixing of the ER and HR resins (r_m). In Eq. 2, $x_E\ (r)$ is the mass fraction of epoxy in a resin as a function of the *r*-value, EW_E is the epoxy equivalent weight (also given by EEW), and EW_H is the hardener equivalent weight, given by the hardener formula weight divided by the number of functional groups. $x_H\ (r)$ is the compliment of $x_E\ (r)$. In Eq. 3, AW_{ER} and AW_{HR} are the resin areal weights of the ER and HR plies, respectively, and $x_H\ (r_{ER})$, $x_H\ (r_{HR})$, $x_E\ (r_{ER})$, and $x_E\ (r_{HR})$ are the mass fractions of hardener and epoxy in each of the ER and HR resins. The resin areal weights were obtained from measurements made during prepreg preparation.

Equation 2: $$x_E\ (r) = \frac{EW_E}{EW_E + rEW_H}$$

Equation 3: $$r_m = \frac{EW_E\left(AW_{ER}x_H\ (r_{ER}) + AW_{HR}x_H\ (r_{HR})\right)}{EW_H\left(AW_{ER}x_E\ (r_{ER}) + AW_{HR}x_E\ (r_{HR})\right)}$$

This report describes the development of AERoBOND materials and processes to maximize mechanical properties of the assembled joint. Experimental variables and controls included the resin *r*-values, ER and HR areal weights, vacuum bagging scheme,

autoclave cure cycle, and reinforcing fiber types. For each test configuration, infrared (IR) spectroscopy was used to measure the chemical state of the ER surface after primary cure to determine if *r*-values changed during primary cure (normally ≤ 0.15). Laminates were then fabricated, inspected ultrasonically, and mechanically tested to measure fracture toughness. Because of the complex interdependence and number of process parameters, an iterative, path-finding approach was used to improve mechanical performance. In addition, process simulations were leveraged to efficiently explore the complex parameter space and suggest new test configurations. The end-notched flexure (ENF) test method provided a rapid assessment of AERoBOND performance because specimen preparation was simple, the method was well established in our laboratories, mechanical testing and post-processing was the quickest compared to the other tests selected for the project, and the mode-II fracture toughness is a good indicator of joint performance [17, 18].

1.4 Considerations for Aerospace Implementation

In composite aircraft structures, adhesively bonded joints often outperform co-cured joints in mechanical testing (where the fracture plane is directed to the adhesive layer) because adhesives are designed to be tougher and stronger than composite matrix resins at a detriment to stiffness. Although adhesively bonded joints can achieve higher structural performance relative to co-cured joints, they remain susceptible to contamination during the fabrication process that may weaken the joint. The inherent reliability and predictability of co-cured (AERoBOND) joints is the critical factor in moving from bonded joints with redundant fasteners to unitized structures with minimal fastener requirements. Therefore, the goal of this investigation is not to compare AERoBOND joints with adhesively bonded joints

nor improve upon the mechanical performance of co-cured joints, but rather to achieve bond performance similar to that of co-cured joints.

The resins and prepregs used for the AERoBOND process are prepared very similarly to the conventional epoxy resin used currently for airframe production. The reliability of the conventional materials is certified by the material manufactures through rigorous screening of each batch prior to delivery. It is the viewpoint of the authors that similar certification screen could be conducted on AERoBOND resins prior to delivery to ensure performance in the end product.

2. EXPERIMENTATION

2.1 Materials and Methods

Epoxy resins were formulated from two components: API-60® (part A) epoxy resin supplied by Kaneka North America with an EEW of 131 g/mol (provided by the manufacturer) and diethyltoluenediamine (DETDA, part B) hardener supplied by Alpha Chemistry, as shown in Figure 2. DETDA has a molecular weight of 178.27 g/mol and a EW_H of 44.6 g/mol based on four reactive functional groups.

Resins were formulated from parts A and B in a resin kettle in 1.2 kg batch size by heating to 100 °C and agitating with an overhead mechanical stirrer for 60-90 min under a nitrogen atmosphere. HR and ER prepreg was prepared from HexTow® IM7G, 12K carbon fiber from Hexcel Corporation® and offset resins with *r*-values of about 0.1, 0.25, 2.5, and 6.7. In some experiments, the HR prepreg was prepared with plain weave carbon fiber tape obtained from Fiber Glast® (part number 693-B) in 45.7 m lengths with a width of 76.2 mm, 3k tows, and a fiber areal weight (FAW) of 198 g/m^2. Methyl ethyl ketone (MEK),

obtained from Sigma Aldrich, was used to dilute the resin for prepreg preparation. Hexply® IM7/8552, 35 wt% resin content (RC), 190 g/m^2 FAW unidirectional tape was obtained from Hexcel Corporation® and used as backing for the fabrication of mechanical test specimens and used to measure baseline co-cure properties.

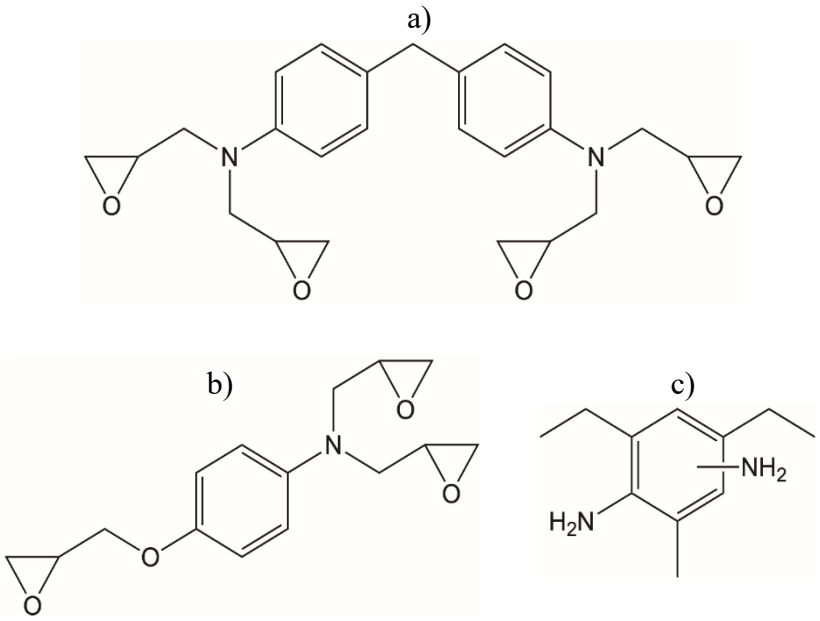

Figure 2. Structures of API-60® epoxy resin including the (a) tetrafunctional epoxy, 4,4′-methylenebis(N,N-diglycidylaniline), (b) the trifunctional epoxy, N,N-diglycidyl-4-glycidyloxyaniline, and (c) the tetrafunctional hardener diethyltoluenediamine (DETDA). Molar ratio of the monomers (a) to (b) was known as 3:1.

Unidirectional and plain weave prepreg tapes were prepared using the NASA Langley Research Center (LaRC) prepregger [19] shown schematically in Figure 3 from a resin solution of 70-85 wt.% solids and the compliment of MEK. In addition to prepregging, HR material was also prepared by hand painting the MEK/HR resin solution (30% to 50%

solids in MEK) onto a plain weave, e-glass fiber fabric. Twenty-three-ply, unidirectional composite panels were prepared by laying up the Hexcel® Hexply® 8552 prepreg, ER prepreg, and HR material in a 30 cm by 15 cm format according to [Hexcel9/ER2/HR/||/ER2/Hexcel10]. The || symbol designates the location of a fluorinated ethylene propylene (FEP) release film, 12.5 μm thick, which was inserted to create a precrack at the center plane of the panel required for mechanical testing. Each panel was cured in an autoclave using the two-step process in Figure 1. Primary cure produced two "half-panels" with following layups: [Hexcel9/ER2] and [Hexcel10/ER2]. The half-panels were then assembled with one or two plies of HR material in contact with the ER surfaces and returned to the autoclave for secondary cure. The hold temperatures and times were varied as part of the experimental method, but the heating and cooling ramp rates were fixed at about 2.8 °C/min.

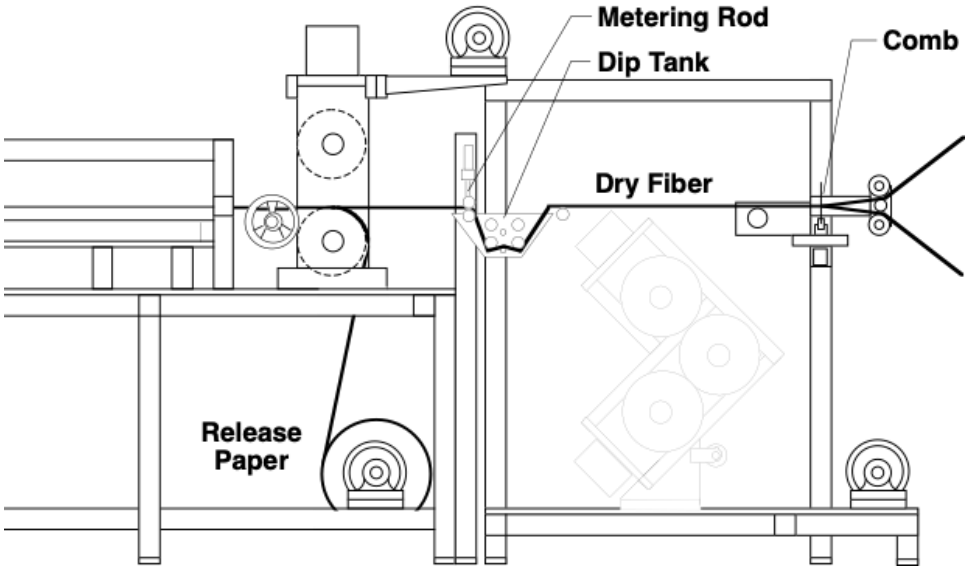

Figure 3. Schematic of NASA LaRC multipurpose prepreg machine using solution coating.

2.2 Fabrication Considerations

Experimental laminates were fabricated using industry standard vacuum bagging methods and materials on flat aluminum tool surfaces. The use of offset resins required some special considerations regarding resin retention and surface texture. Because the offset resins are designed to not vitrify during the primary cure cycle, all parts were enclosed in an impermeable envelope made using 50 μm thick FEP (Airtech, A4000V) release film and 25 mm wide medium-tack, flash breaker tape (Airtech, Flashbreaker® 1). Edge dams made from Airtech Airdam 1 tape were placed around the perimeters of all parts outside of the FEP envelope to further prevent resin bleed. The ER surface of the part was placed in contact (through the FEP envelope) with the tool surface to achieve a smooth finish. The tool finish on the ER surface was hypothesized to reduce the extent of resin re-flow and displacement required to achieve complete wetting between the ER and HR surfaces during secondary cure. Caul plates (steel, 5 mm thick), permeable release fabric (release ease), and breather blanket (Airtech, Ultraweave® 1332) were placed over the part prior to sealing the bag (Airtech, Ipplon® DP1000) with vacuum bag tape (Airtech, GS-43MR). Figure 4 shows how appears of the laminates at several stages of the layup and assembly process.

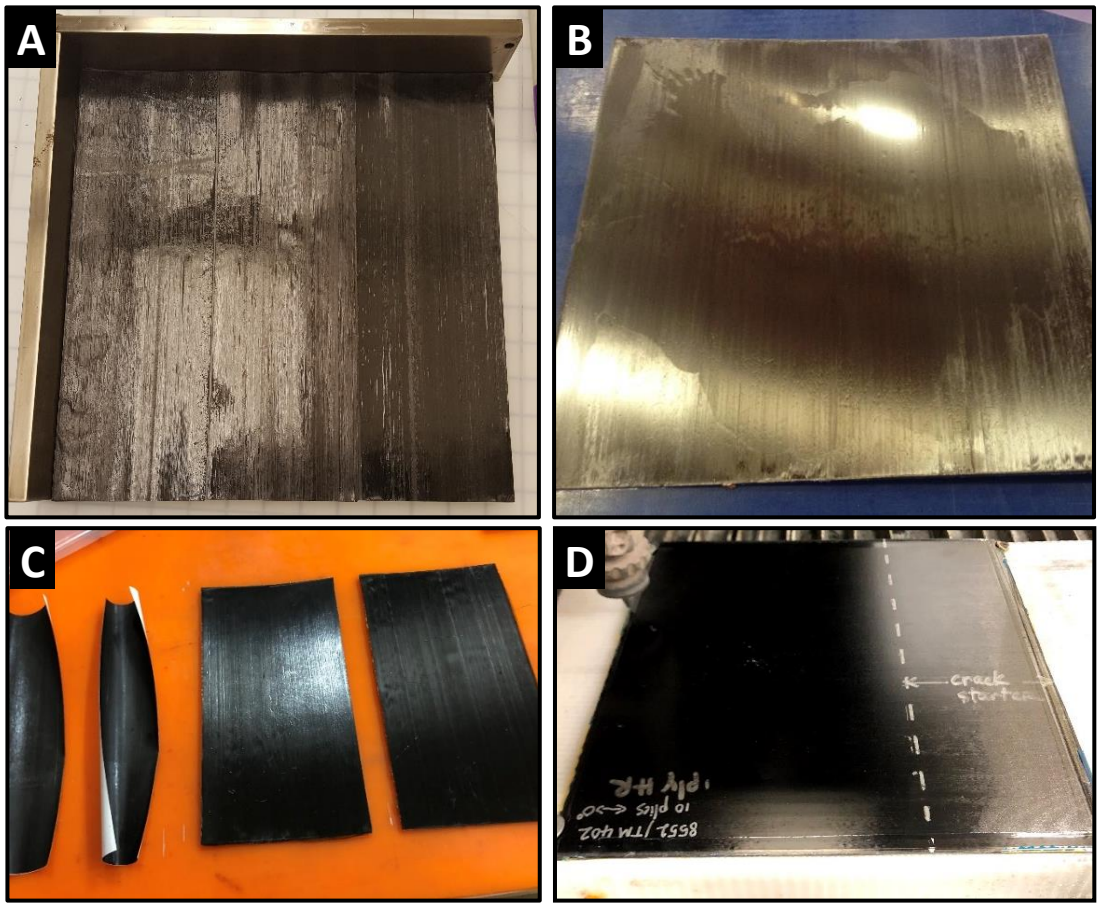

Figure 4. Photos from the manufacturing process showing A, ER prepreg laid up on the conventional backer prior to cure (the steel tool was used to improve ply alignment during hand layup); B, a the ER surface of a laminate after primary cure but prior to assembly; C, HR prepreg plies and ER panels ready for assembly; and D, a finished panel after secondary cure (the dashed line indicates the location of the crack starter film). The fiber direction is top to bottom in all pictures except picture D, which is left to right.

2.3 Characterization and Analysis

Differential scanning calorimetry (DSC) was conducted on offset resins using a TA Instruments Q20 modulated DSC (MDSC®) with a heating rate of 3 °C/min. Samples of approximately 3 mg were hermetically sealed in aluminum pans and cured at 180 °C for 2

h before cooling to -60 °C and ramping to 280 °C to measure the glass transition temperature (T_g) and residual heat of reaction.

Resin chemistry was characterized by IR spectroscopy using a Thermo-Nicolet iS5 Infrared Spectrometer equipped with an iD7 ATR diamond optic accessory. The *r*-values were calculated based on the relative peak heights at 907 (epoxy-specific; epoxide ring) and 1450 cm^{-1} (hardner-specific; N-substituted aromatic C-C of DETDA), normalized against 1514 cm^{-1} (strongest peak in most spectra; aromatic C), using an empirical calibration curve developed from a series of resin samples of known *r*-values (in the range of 0.1 to 7) and degrees of cure. The calibration curve (Figure 5) indicated a linear correlation in the entire *r*-value range between Log(*r*) and the difference of the normalized peak intensities at 907 cm^{-1} and 1450 cm^{-1} given in Eq. 4. The coefficients were determined by least squares, linear regression. Eq. 5 was used to estimate the *r*-value of cured resins of unknown composition based on IR spectral data (r_{IR}).

Equation 4: $$-0.463\,Log(r) - 0.067 = 3\,I_{907\ cm^{-1}} - I_{1450\ cm^{-1}}$$

Equation 5: $$r_{IR} = 10^{\frac{3I_{907\ cm^{-1}} - I_{1450\ cm^{-1}} + 0.067}{-0.463}}$$

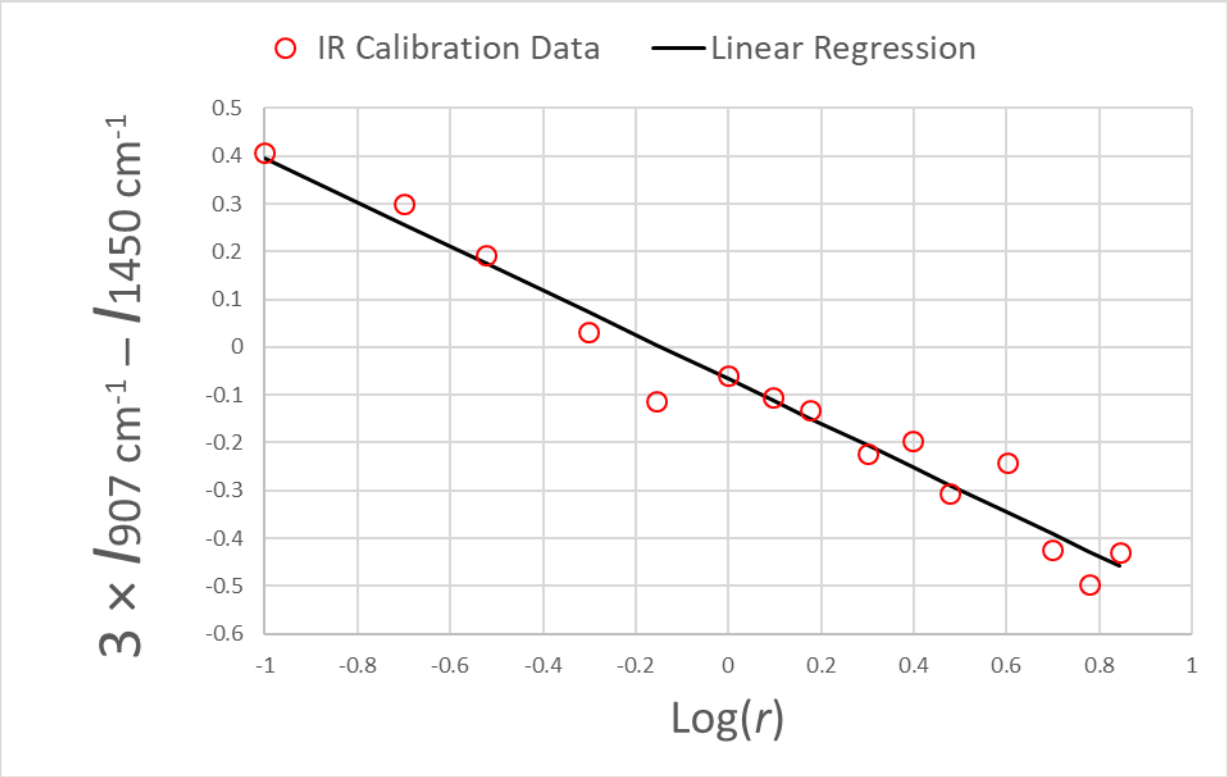

Figure 5. Linearized calibration curve relating the *r*-value to select IR peak intensities of arbitrary units. The intensities (*I*) of the two selected peaks (907 and 1450 cm^{-1}) were normalized against that of 1514 cm^{-1}.

Ultrasonic inspection in pulse-echo mode was conducted on a MISTRAS® UPK-T60-HS high speed C-scan system fitted with a NDT Automation® 10.0 MHz/13 mm immersion transducer (IU10G1).

After panels underwent their initial C-scan, test specimens were then cut from panels using a waterjet. Due to the nature of the waterjet cutting process, the initial pre-crack in weakly bonded specimens would occasionally delaminate partially (or completely in rare instances) prior to any testing (i.e. specimens damaged by cutting process). To ensure valid specimens were tested, each one was inspected ultrasonically again after machining to

confirm that the specimen's integrity had not been compromised (i.e. crack front had not extended from the FEP insert) as shown in the top images of Figure 6. The side edges of intact specimens were then lightly polished to reduce out-of-plane stress concentrations (i.e. deep scratches formed from the waterjet cuts), which can cause premature failure on the edges and, via cascade, the entire specimen.

In order to inspect joints in the panels, sample specimens were polished using a Nano 1200T grinder-polisher (Ace Technologies). Silicon carbide papers (grit size of 400, 600, 800, and 1200) and polishing suspension (alumina, 0.05μm, Buehler) were used to make a mirror surface. The polished sample surfaces were imaged using an optical microscope (DM 800M, Leica) installed with a 5 Megapixel CCD camera (DFC450, Leica).

The same specimens were inspected by IR microscopy using a Bruker LUMOS II FT-IR Microscope equipped with a retractable ATR crystal probe and a motorized stage. In a typical scan, the mapping area was 1.5×0.45 mm^2, where 1000×30 spectra were acquired with each spectrum collected from an area of 15×15 μm^2. Post-processing of the spectra was performed using in-house python scripts with the NumPy [20], SciPy [21], and Matplotlib [22] libraries to facilitate automated processing and visualization of the large datasets. The spectra were baseline corrected using a "rubberband" method by finding the convex hull [23] and normalized against the aromatic C-C peak at ~1515 cm^{-1}. Contour maps were then generated by integrating designated peaks of interest. Data reported here used the peak integrations at ~1614 and ~1293 cm^{-1}, which could be assigned to the amine groups of DETDA (specific to HR-ER regions) and sulfone group of DDS (specific to conventional resin), respectively. Peak areas were calculated by integrating over the peak

region using the trapezoid rule, subtracting a baseline calculated using the rubberband method applied over only the peak region. The peak regions were defined as 1595-1630 cm^{-1} for the DETDA peak and 1260-1315 cm^{-1} for the DDS peak.

ENF testing was conducted according to ASTM D7905-14 to measure mode-II fracture toughness using six replicate specimens per plate [17]. Figure 7 shows the test configuration using a 3-point bend fixture to load the specimen. Prior to testing, width and thickness measurements were taken using a pair of calipers as per specifications in ASTM D7905-14; occasionally specimens which came from the edges of the panels failed to meet the thickness-variation tolerance. The vacuum bag during cure would compress the edges of the panels more so than the central area which caused specimens from the edges of the panel to exhibit a considerably thinner side than the other when traveling across the width of the specimen. If placed in the 3-point bend test fixture, the thicker side would be loaded before the thinner side and a non-uniform loading state would cause non-self-similar crack growth (i.e. crack would grow unevenly across the specimen width) which negates the assumptions inherent in the equations used to calculate the fracture toughness. Yet, even specimens which measured up to the testing requirements were not guaranteed to produce valid results. Extra considerations were necessary to be satisfied before measured material properties were considered valid which are discussed hereafter.

The ENF test is conducted in two phases. In the first phase, the delamination is extended from the manufactured crack tip, which had been fabricated from the FEP insert. The manufactured crack tip is relatively blunt in comparison to a natural crack tip. Because of this ‘bluntness’ the stress-concentration at the crack tip is lower than that from a natural

crack tip, which requires a greater crack driving force than normal to grow the delamination. Hence fracture toughness measurements from the first test are overestimates of the true value. However, once the delamination has grown from the first test, the crack tip has naturally become microscopically sharp. The new, natural crack tip is then used in the second phase of ENF testing. Because the specimen is considered to have been previously cracked in the first phase, the specimen for the second phase is described as precracked (PC). Based on this nomenclature, the untested specimen in the first phase with a manufactured crack tip is known as non-precracked (NPC). Because of variability in the fabricated crack tip from the FEP insert, test results from NPC tests generally exhibit greater variability, while PC tests usually generate more consistent findings along with more conservative fracture-toughness values because the sharper crack tip provides a more singular stress concentration. Fracture toughness values from the PC test are typically used in structural design applications; however, results from NPC tests in this campaign are also valuable because they supply more comparisons with previous fabrication parameters and provide additional insights.

Each specimen was C-scanned after its NPC test as well as its PC test to judge the validity of the just-obtained test results as presented in Figure 6. If the delamination had migrated to another interface (i.e. another interface begins to delaminate) or if the crack front had grown non-uniformly to a significant degree, the results were deemed invalid. The rigorous process of rooting out valid test data provides confidence in the reported fracture toughness measurements contained herein.

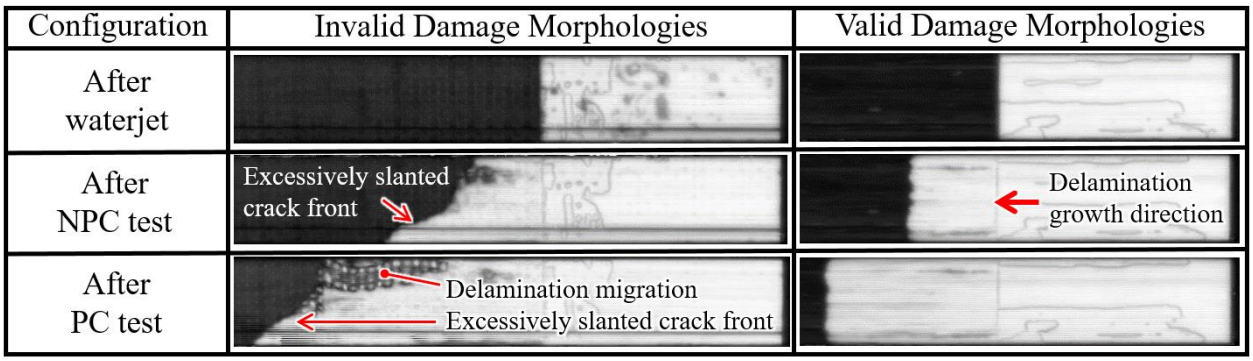

Figure 6: C-scans of ENF specimens throughout the testing process which demonstrate contrasting damage morphologies that produce valid and invalid test measurements. Delaminated portions appear white while portions of the specimen which are still intact appear black.

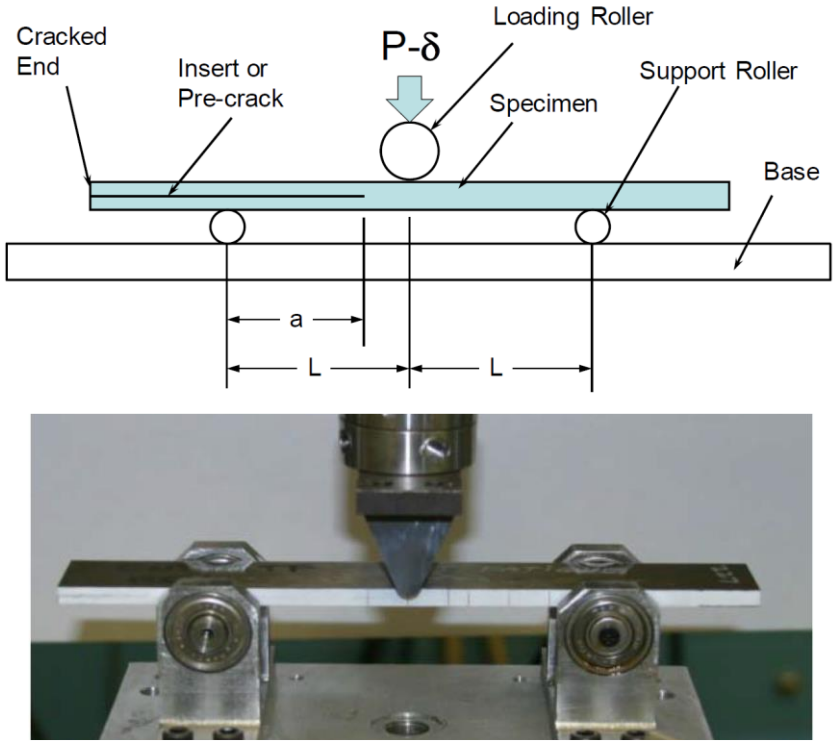

Figure 7. Specimen schematic and a photograph of test setup for the ENF test take from [18].

3. RESULTS

Preliminary process development, published previously, led to the approximate resin compositions, cure cycle parameters, and bagging schemes described herein [14, 15, 24, 25]. Critical findings from several preliminary experiments are summarized in Section 3.1. A high-level overview of the process simulations used to supplement the process development is given in Section 3.2. Detailed results from four experiments are presented in Sections 3.3-3.7 where *r*-values for the ER and HR resins were 0.1 or 0.15 and 2.5, respectively.

3.1 Preliminary Process Development

Preliminary experiments indicated that extremely high hardener concentrations ($r > 5$) and crystalline solid hardeners (DDS) hampered diffusion and bonding in the secondary cure process. During the primary cure, the ER resin at the surface must not advance past the gel point (~45% conversion for this system) to maintain the mobility needed to affect mixing during the secondary cure. The *r*-value of the ER surface, inferred from IR spectral analysis (Table 1), indicates the relative advancement of the surface polymer due to ingress of hardener from the bulk of the laminate or homopolymerization of the epoxy. ER surfaces with *r*-values less than ~0.3 resulted in measurable joint properties whereas those with *r*-values greater than ~0.3 (data not included here) formed no joints. Early testing indicated that the ER layer required a minimum fiber areal weight (>70 g/m^2, FAW per ER ply) and resin content (~55% RC) to remain sufficiently flowable and reactive after the

primary cure. Further, the final hold time at 178 °C was limited to 1 h to prevent excessive etherification of the ER matrix.

3.2 Process Simulations

Process simulations were untaken concurrently with experiments to aid a more thorough investigation of the complex parameter space. A one-dimensional model was implemented to represent the layup of the conventional, ER, and HR resins and implicit finite difference methods were used to evolve the systems according to the primary and secondary cure cycles. The governing equations for heat transfer, mass transfer, and resin cure were calibrated with available experimental data. Model simplicity was prioritized to allow rapid screening of thousands of configurations while varying parameters related to the prepreg and cure cycles. By filtering the high-throughput screening using desired process criteria, the most promising configurations were identified and tested. For instance, a low degree of cure (DoC) at the surface following the primary cure favored resin reflow and intermixing during the secondary cure. Details of the model development and simulation results will be published in a separate report.

3.3 Experimental Data Summary

Table 1 summarizes the results and process parameters for seven selected test configurations. The top portion of the table shows mechanical performance characteristics based on mode-II fracture toughness, G_{IIc}, and is compared to the performance of conventional, co-cured laminate. The second section of the table provides formulation details for the ER and HR precursors used to fabricate joints. The bottom section of the table summarizes the autoclave cure cycles for primary and secondary cure. Included here

is the estimated r_{IR}-value of the ER surface post primary cure, which was obtained by IR inspection of the ER surfaces prior to assembly. For configuration 6, the cure process was determined by process simulations, which is why its cure cycle parameters are notably different from the others.

Table 1. Test parameters and results from seven test configurations are summarized. The baseline fracture toughness used to calculate G (% baseline) was 855 J/m^2 [18]. ER r-values were measured after primary cure.

	Test Configuration						
Test Factor/Result	**1**	**2**	**3**	**4**	**5**	**6**	**7**
Qual. Performance	no bond	Low	Med./Low	Med.	Med./High	High	High
G (% baseline)	0	5	33	46	73	101	107
G_{IIc} (J/m^2)	0	43	280	396	620	862	920
	ER and HR Prepreg Parameters						
ER r-value	0.15	0.15	0.15	0.1	0.15	0.1	0.1
ER RC	48%	63%	60%	63%	66%	63%	63%
ER FAW (g/m^2)	195	60	70	77	77	77	77
ER Fiber	PW	UD	UD	UD	UD	UD	UD
ER # of plies	1	**2**	**2**	**2**	**2**	**2**	**2**
HR r-value	2.5	2.5	2.5	2.5	2.5	2.5	2.5
HR RC	47%	77%	52%	47%	49%	49%	46%
HR FAW (g/m^2)	195	75	76	195	78	78	195
HR Fiber	PW Fabric	Glass Scrim	UD	PW Fabric	UD	UD	PW Fabric
HR # of plies	1	1	1	2	2	1	1
	Cure Cycle Parameters and r_{IR}-Value Estimated from IR Spectrum						
Prim. Hold 1 (min)	180	N/A	180	180	180	150	180
Prim. Hold 1 (°C)	107	N/A	107	107	107	121	107
Prim. Hold 2 (min)	60	120	60	45	45	180	45
Prim. Hold 2 (°C)	178	178	178	178	178	135	178
r_{IR}-value	0.16	0.34	0.18	0.14	0.14	0.12	0.15
Sec. Hold 1 (min)	60	60	60	60	60	15	60
Sec. Hold 1 (°C)	107	107	107	107	107	138	107
Sec. Hold 2 (min)	240	240	240	240	240	180	240
Sec. Hold 2 (°C)	178	178	178	178	178	171	178

The results in Table 1 are arranged from left to right in increasing joint performance as indicated by the mode-II fracture toughness. Some general conclusions can be drawn from the summary in Table 1. Thicker ER layers with higher resin content tend to result in increased performance. Lower *r*-value estimated from the post primary cure inspection correlates with improved mechanical performance as well. Both observations indicate that ER layers with reduced degree of cure (DoC) and sufficient resin to reflow and achieve intimate contact and mixing with the HR layer during secondary cure is critical to achieve high performance. The r_m value was calculated for each test configuration in Table 1 using Eq. 3, and the results are shown in Table 2. Other than the outlier for test configuration 3, toughness appears to increase with deceasing r_m. The r_{IR}-value was elevated for test configuration 3 indicating that the ER resin either flashed from the laminate surface due to an improper edge dam or the primary cure cycle caused excessive advancement of the DoC. Either case would reduce the extent of mixing during secondary cure and reduce mechanical performance as was observed. The combination of low r_{IR} ($\leq$0.15) and r_m ($\leq$0.8) values in test configurations 5-7 resulted in high mechanical performance. Although the r_m-value was not a predetermined process parameter for these tests, these results indicate it should be controlled in future experiments to improve process control.

Table 2: Theoretical r_m-values for fully mixed HR and ER resins calculated using the data in Table 1 and Equation 3.

Test Configuration	**1**	**2**	**3**	**4**	**5**	**6**	**7**
Theoretical mixed r-value (r_m)	0.98	1.12	0.58	1.12	0.67	0.43	0.73

The highest performing test configurations exceeded the baseline toughness. These test configurations were replicated in subsequent experiments to measure additional mechanical properties with relevance to cocured joints: mode-I fracture toughness, interlaminar tensile strength, interlaminar shear strength, and damage tolerance (via barely visible impact damage and compression after impact testing). Results from these investigations will be published in a subsequent report.

3.4 Non-destructive Inspection

Select images obtained from ultrasonic inspection are shown in Figures 8-10. The amplitude C-scan images show the highest amplitude signal reflected from the joint region. Acoustic reflections are caused by variations in acoustic properties of the material that may indicate subtle variations in material composition (weak reflections) or voids, disbonds, and foreign debris (strong reflections). Strong reflections (orange and red colors) from the joint region strongly indicate the joint may not meet baseline performance specifications. The time-of-flight (ToF) C-scan images indicate where in the part the strongest reflections originate. The image scaling is set such that reflections from the backside of the laminate appear in yellow (correlates with maximum thickness) and reflections from the mid-plane (near the joint) appear blue.

The B-scan images provide a cross-sectional view of the laminate at the location of the red cursor on one of the C-scan images, as indicated in each caption. The color of the B-scan indicates the strength of the reflected amplitude, which ranges from -100% to 100%. In the B-scan image, the location and severity of defects through the thickness can be visualized as well as distortion or curvature of the laminate.

In Figure 8, the amplitude and ToF C-scan images from test configuration 2 clearly show the precrack regions as red and blue rectangular regions at the right end of the image, respectively. The C-scan images also show large red areas (amplitude scan) and blue areas (ToF scan), which indicates the joint has significant void defects due to poor consolidation. The ultrasonic inspection results correlate well with the poor mechanical performance measured from samples made from this laminate.

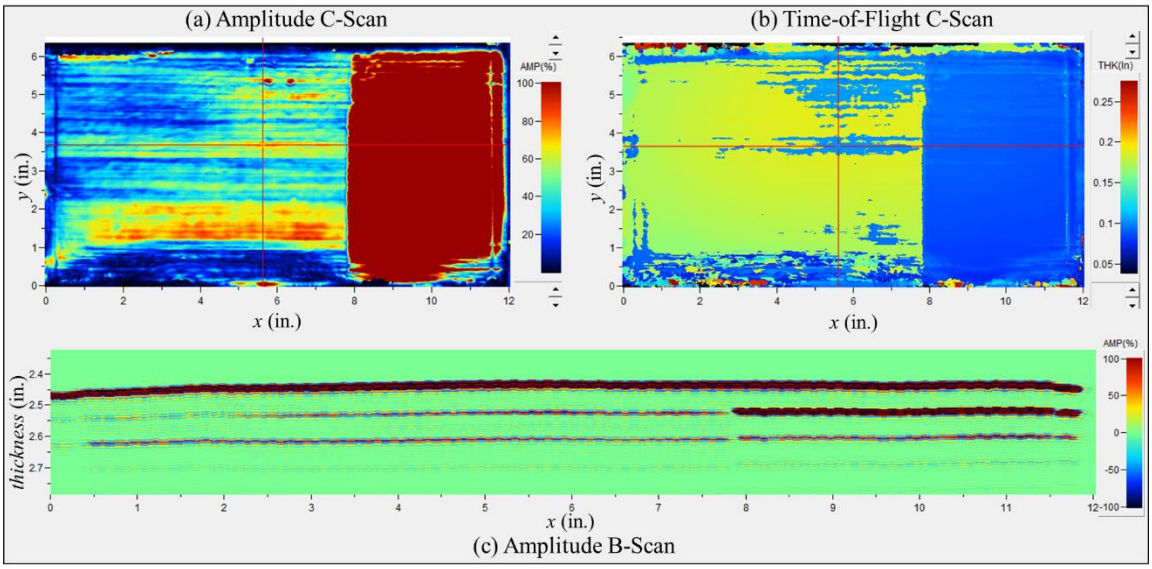

Figure 8. Ultrasonic inspection results from test configuration 2. Image (a) shows the maximimum amplitude reflected from within the laminate, image (b) shows the origin through the thickness most intense reflection, and image (c) show the B-scan image take at the location of the cursor in (a).

Figure 9 shows the ultrasonic inspection results for test configuration 4. The manufactured precrack is visible in the rightmost third of the laminate. The amplitude C-scan appears to indicate non-uniformity in the precrack, which is due to warping across the

15 cm dimesion of the panel. Warpage was mostly limited to the precrack area of the panel. It is believed that the plain weave fabric used in the HR-ply of this configuration led to residual stresses that were unbalanced in the precrack region.

The amplitude and ToF C-scan images in Figure 9 show most defect regions are localized at the edges of the laminate. The B-scan also shows a significant disbond in the joint plane, but it is located at the left most edge of the laminate and was not part of any mechnical test specimen. The minor defects seen throughout the field of the laminate indicate flow and consolidation occurred partially but was not complete. These data correlate well with the moderate mechanical performance measured from test configuration 4.

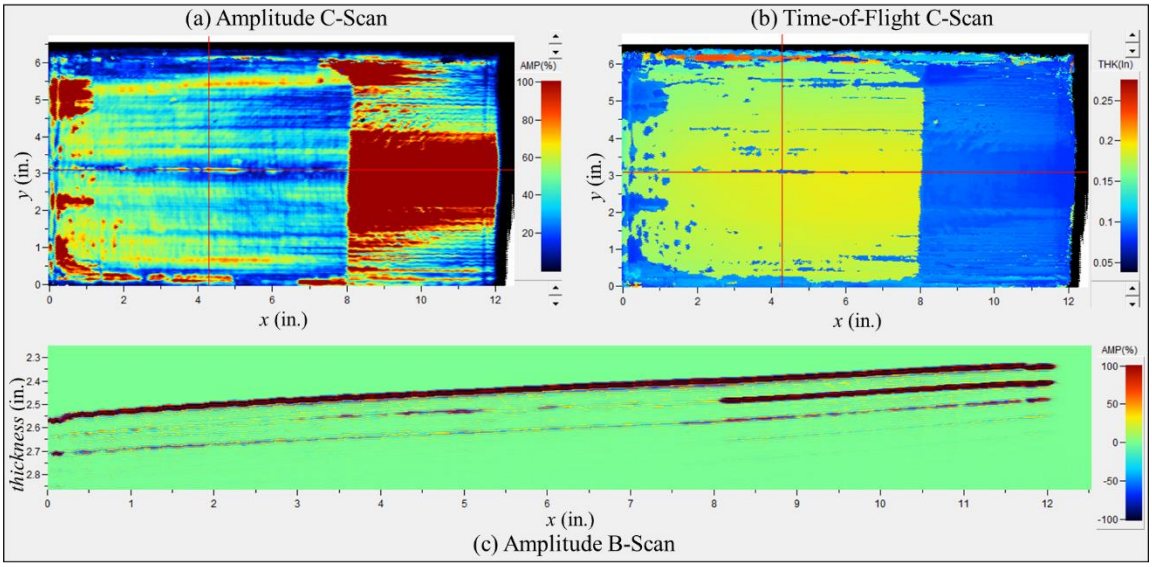

Figure 9. Ultrasonic inspection results from test configuration 4. Image (a) shows the maximimum amplitude reflected from within the laminate, image (b) shows the origin through the thickness most intense reflection, and image (c) show the B-scan image take at the location of the cursor in (a).

The ultrasonic inspection results from test configuration 6 are in shown in Figure 10. The precracks are visible again on the right third of the C-scan images. Nearly no defects were detected in the full field of the joint in both C-scan images. Further, the minor defects marked by the cursors in both C-scans were found to be isolated in the half-panel laminates away from the plane of the joint. The B-scan image taken from the ToF C-scan cursor shows the most prominent defect is located near the top surface of the laminate. These data indicate excellent consolidation at the joint plane, which is born out in the high performrmance measured from mechanical test specimens.

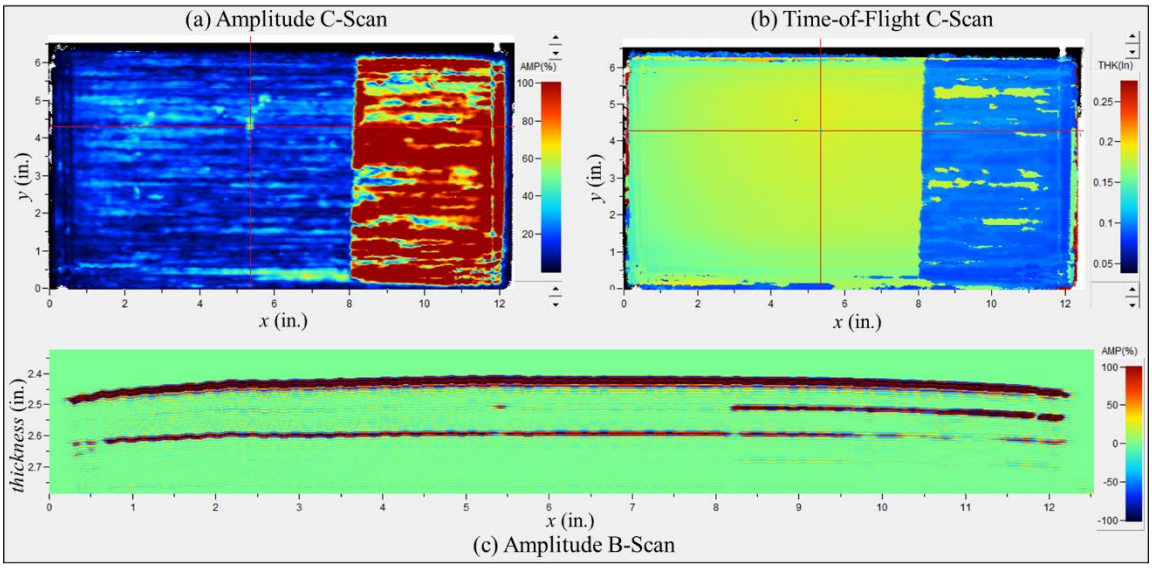

Figure 10. Ultrasonic inspection results from test configuration 6. Image (a) shows the maximimum amplitude reflected from within the laminate, image (b) shows the origin through the thickness most intense reflection, and image (c) show the B-scan image take at the location of the cursor in (a).

3.5 Optical Microscopy

Cross section optical micrographs are presented to visualize the joint. The micrographs evidence the extent of resin mixing and fiber bedding at the interlaminate regions between the HR and ER plies. In Figure 11, the micrographs collected from test configuration 2 show that fibers in the ER plies were not displaced during the secondary cure into the HR resin. Although the color variation is subtle in these micrographs, there is a sharp discontinuity visible in the matrix resin at the HR/ER interface. This discontinuity indicates that little or no resin intermixing occurred during secondary cure, which explains the poor mechanical performance of test configuration 2.

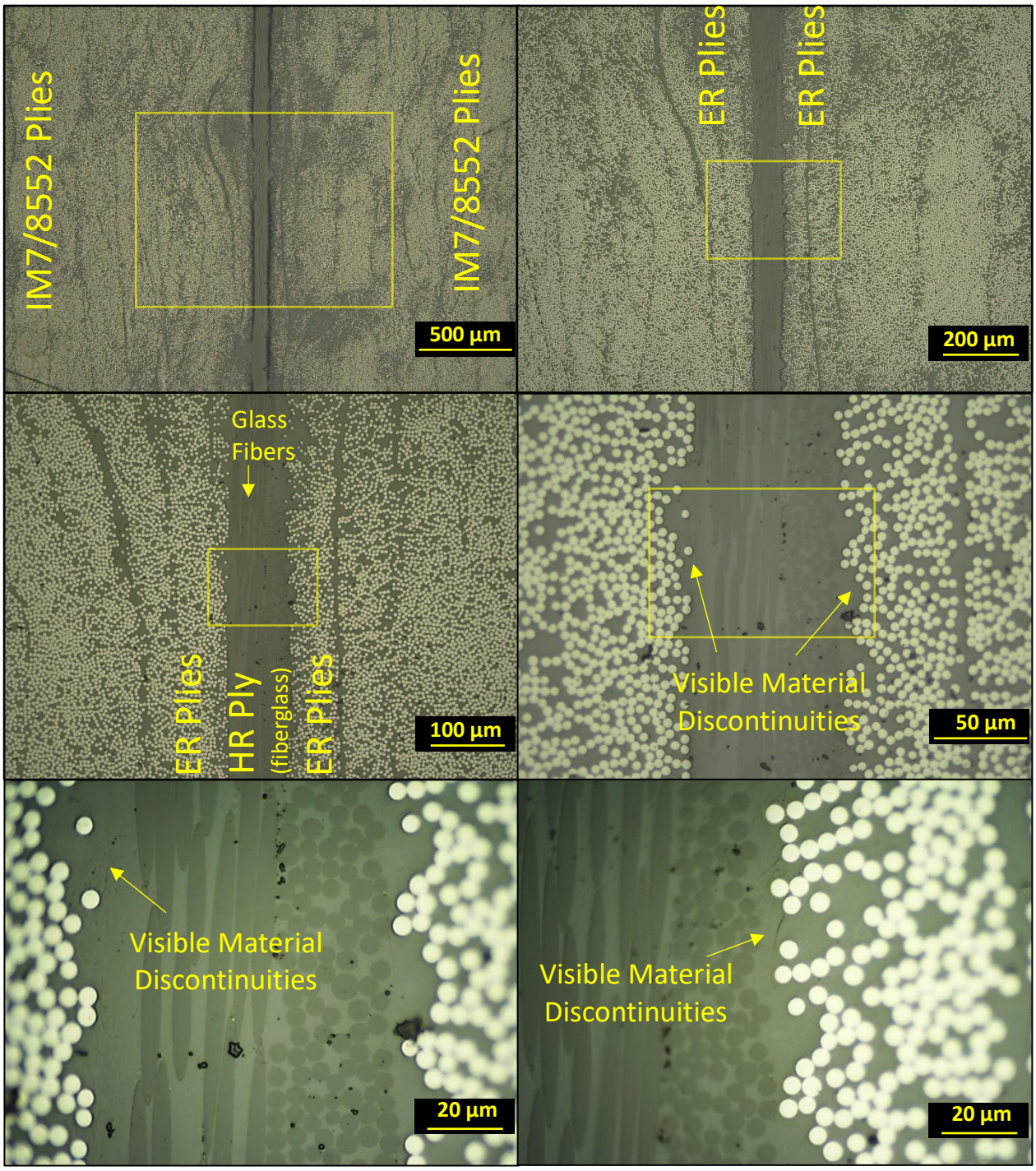

Figure 11. Optical cross section images at multiple magnifications collected from test configuration 2.

Figure 12 shows micrographs from test configuration 4. From the lower magnification images, it can be seen that no carbon fibers migrated out of the ER ply surface into the HR ply during secondary cure. Closer examination of the ER to HR interface reveals a dark line along the interface, which is believed to be a crack due to inadequate reflow of ER resin and residual stress in the laminate due primarily to the unbalanced orthogonal tows of the plain weave HR ply. At the highest magnification, it is also possible to see a subtle color change in the matrix resin at the ER/HR interface. Test configuration 4 exhibited moderate mechanical performance, and is consistent with the micrographs in Figure 12, which indicate insufficient mixing at the interface. It is likely that the specimen used to collect the micrographs of test configuration 4 contained disbonds as shown in the left side of the C-scan images of Figure 9 which is where specimen was cut from.

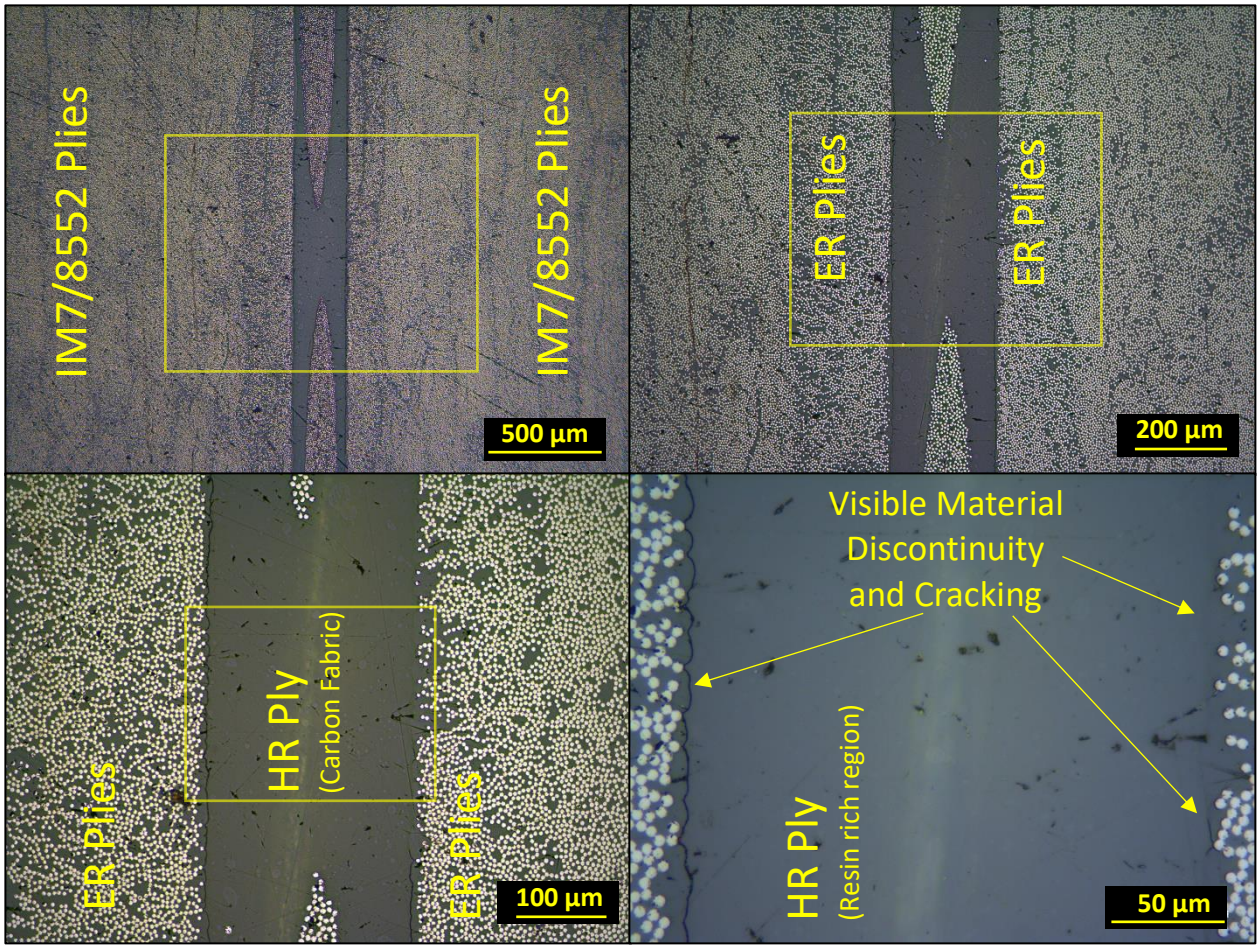

Figure 12. Optical cross section images at increasing magnifications collected from test configuration 4. Yellow rectangles indicate the region of interest shown at the next higher magnification level.

Figure 13 contains the micrographs collected from test configuration 6. The micrographs show that fibers were able to migrate across the ER/HR interface during secondary cure indicating that the ER resin underwent convective flow. High magnification images show no variation in resin color, matrix resin discontinuities, or microcracks. These observations are consistent with effective resin intermixing during secondary cure and the high mechanical performance measured from test configuration 6.

Recall that this configuration was proposed based on the process simulations, where a low DoC in the ER surface following the primary cure was sought to allow for adequate resin reflow and intermixing.

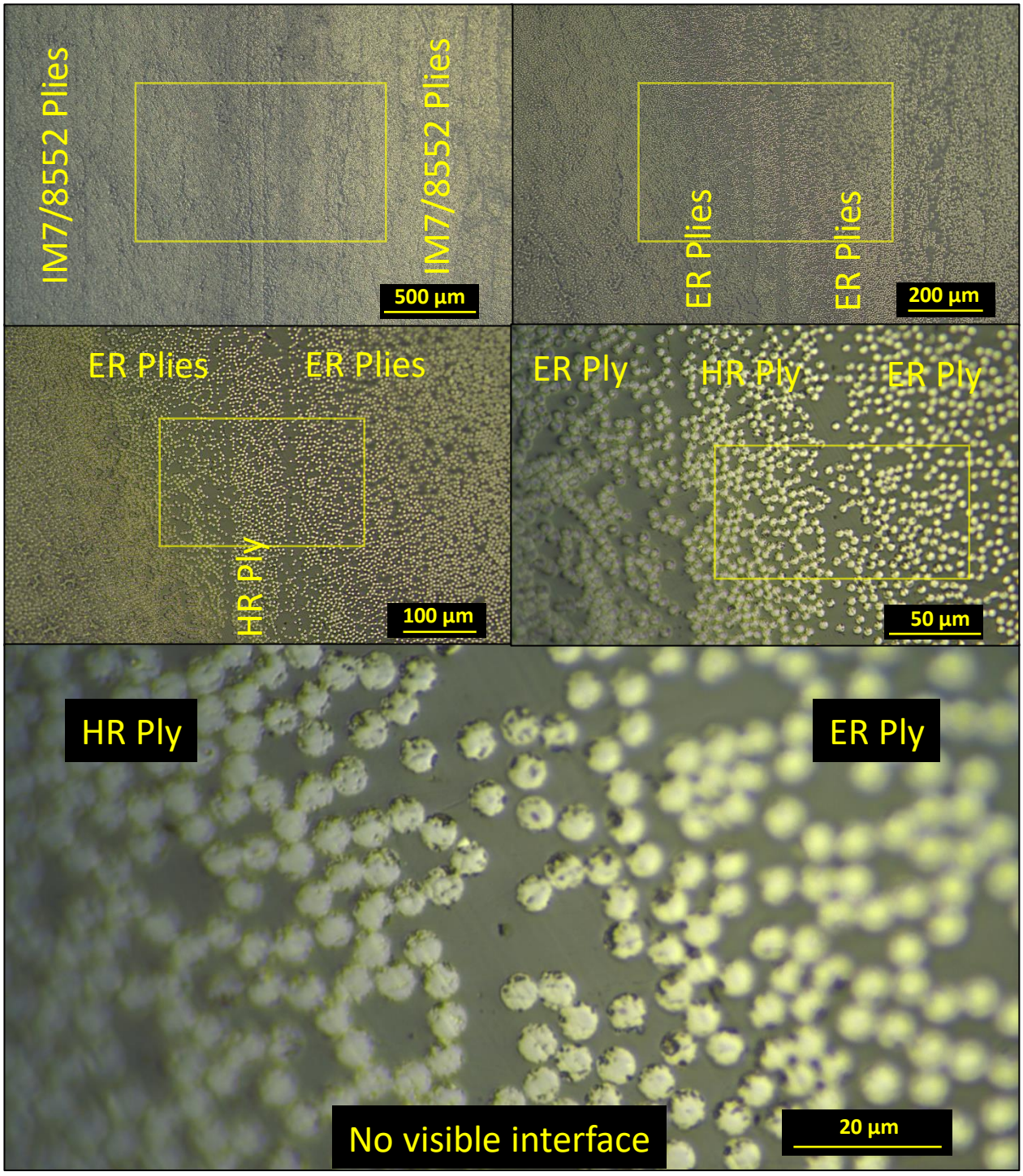

Figure 13. Optical cross section images at increasing magnification take from test configuration 6 (see Table 1). Yellow rectangles indicate the region of interest shown at

the next higher magnification level. In this configuration, the joint shows no visible material discontinuities and fibers from HR and ER layers appear to have migrated into and across the interlaminar region.

3.6 Infrared Microscopy

FTIR-ATR microscopy provided a means to visualize the composition of the matrix resin through the thickness of the joints after final (secondary) cure. The objective of this characterization technique was not to qualitatively observe variation in the *r*-value at each point across the joint from the conventional material through the ER and HR plies. Figure 14 shows the results for test configurations 2, 4, and 6 corresponding to low, medium, and high mechanical performance, respectively. The micrographs in row a show the region of the cross section where the FTIR microscopy data was collected. Rows b and c indicate the diffusional mass transport of the DETDA hardener and the DDS hardener, respectively. During primary cure, the DDS hardener (row c) from the conventional resin diffuses into the ER ply while DETDA (row b) counter diffuses into the conventional resin. During secondary cure, DETDA diffuses from the HR ply to the ER ply. Configurations 2 and 4 (weak and medium performers) both indicate high concentrations of DETDA hardener remaining in the HR ply after secondary cure. The green strip at the center of the HR ply in row b, configuration 4 is not a reduction in DETDA due to diffusion but rather a dense bed of carbon fibers, which can be seen in the micrograph in row a. The limited diffusion of DETDA from the HR ply likely resulted in a brittle HR layer or a weak interface, which resulted in poor fracture performance. For configuration 6, the DDS and DETDA hardeners diffused sufficiently during cure to create the gradual intensity changes seen in

rows b and c. The average signal intensity plots in row d clearly show the steep changes in chemical concentration that occur primarily at the ER/HR ply interface for configurations 2 and 4. The flatter curves in configuration 6 (with less abrupt changes relative to 2 and 4) indicate better mixing at all material interfaces, which likely led to improved mechanical performance.

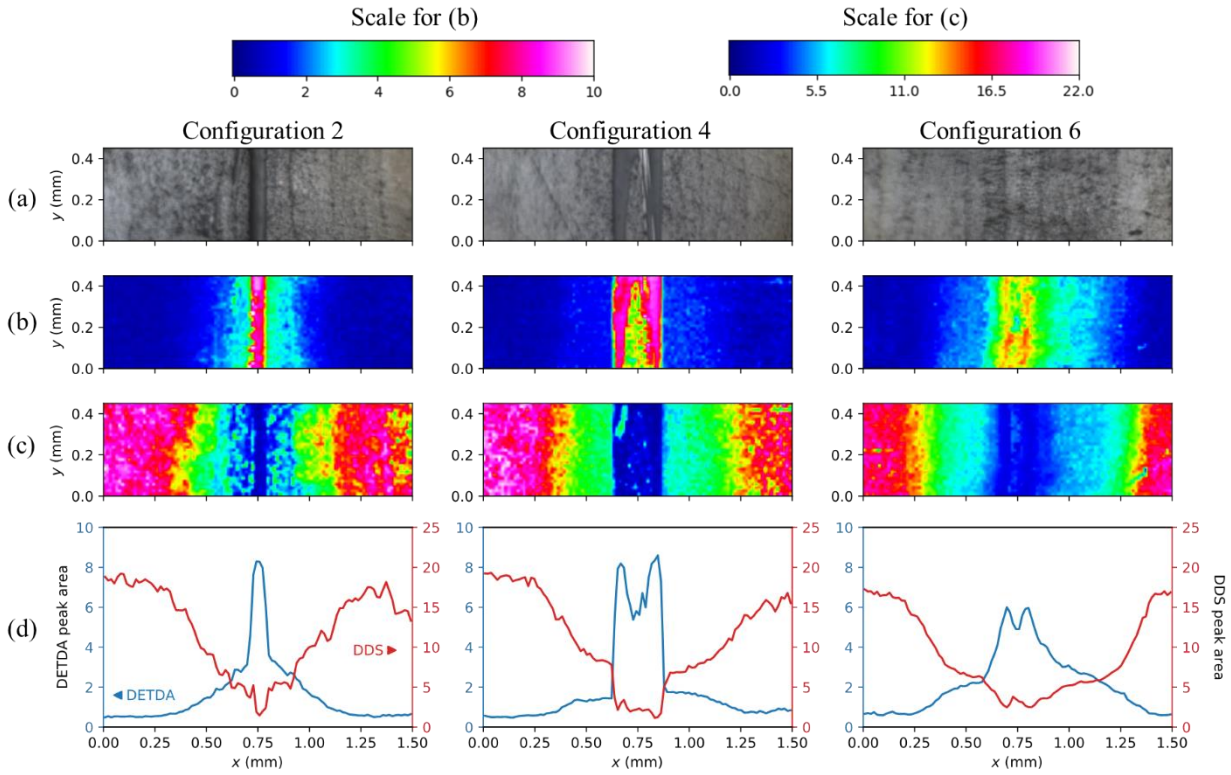

Figure 14. Summary of FTIR microscopy results. Row (a) shows optical micrographs of the joint cross-section with the HR ply at the center of the image. Row (b) is the signal intensity map for the peak at 1614 cm^{-1} arising from the DETDA hardener in the ER ad HR plies. Row (c) is the signal intensity map for the peak at 1293 cm^{-1} arising from the DDS hardener in the conventional material. Row (d) is a plot of the average signal intensity from analysis of the intensity maps in rows (b) and (c).

Figure 15 shows an overlay of the DETDA plots from Figure 14. The overlay shows that the concentration of DETDA decreased significantly in the HR ply for configuration 6 relative to 2 and 4. This confirms that the local concentration of hardener in the HR ply decreased dramatically during secondary cure due to effective reflow into neighboring ER plies, which is a critical factor for developing mechanical performance in the joint.

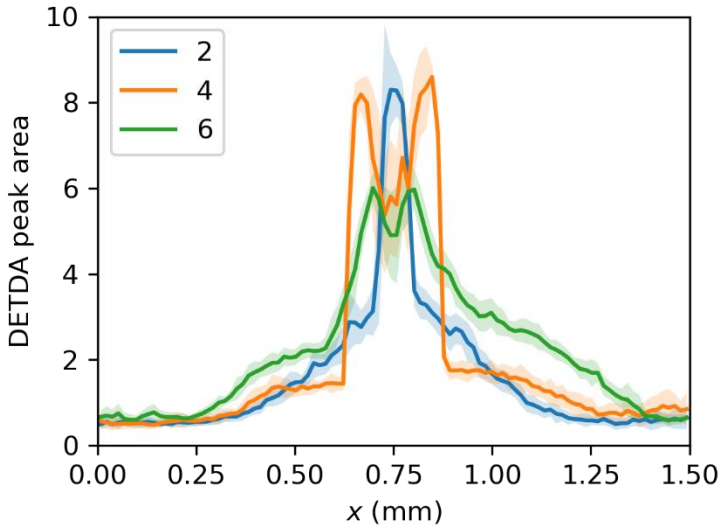

Figure 15. Overlay of average signal intensity plots. Numbers in the legend indicate the test configuration for each trace. The shaded areas indicate the uncertainty in measured intensity.

3.7 Mechanical Performance Assessment

Mode-II fracture toughness values for configurations 4-7 reported in Table 1 were gathered from the specimens whose UT scans from before and after each test are displayed in Figure 16. UT scans for configurations 1-3 are not presented due to the following limitations. Specimens from configuration 1 completely delaminated from the waterjet process and could therefore not be scanned or tested. Specimens from configurations 2 and

3 completely delaminated from the NPC test and therefore NPC and PC scans were unattainable. In some cases, the crack morphology after the NPC test invalidated the NPC test data, but it was still possible to measure valid PC test data from the same specimens. Configuration 6 demonstrates this principle; damage morphology post NPC tests invalidated the NPC results yet the results from the PC tests were valid. Also notice that as fracture toughness increases (going from configurations 4 to 7) the crack fronts become less slanted and become increasingly more uniform (i.e. straight) across the specimen width which increasingly validates the obtained data.

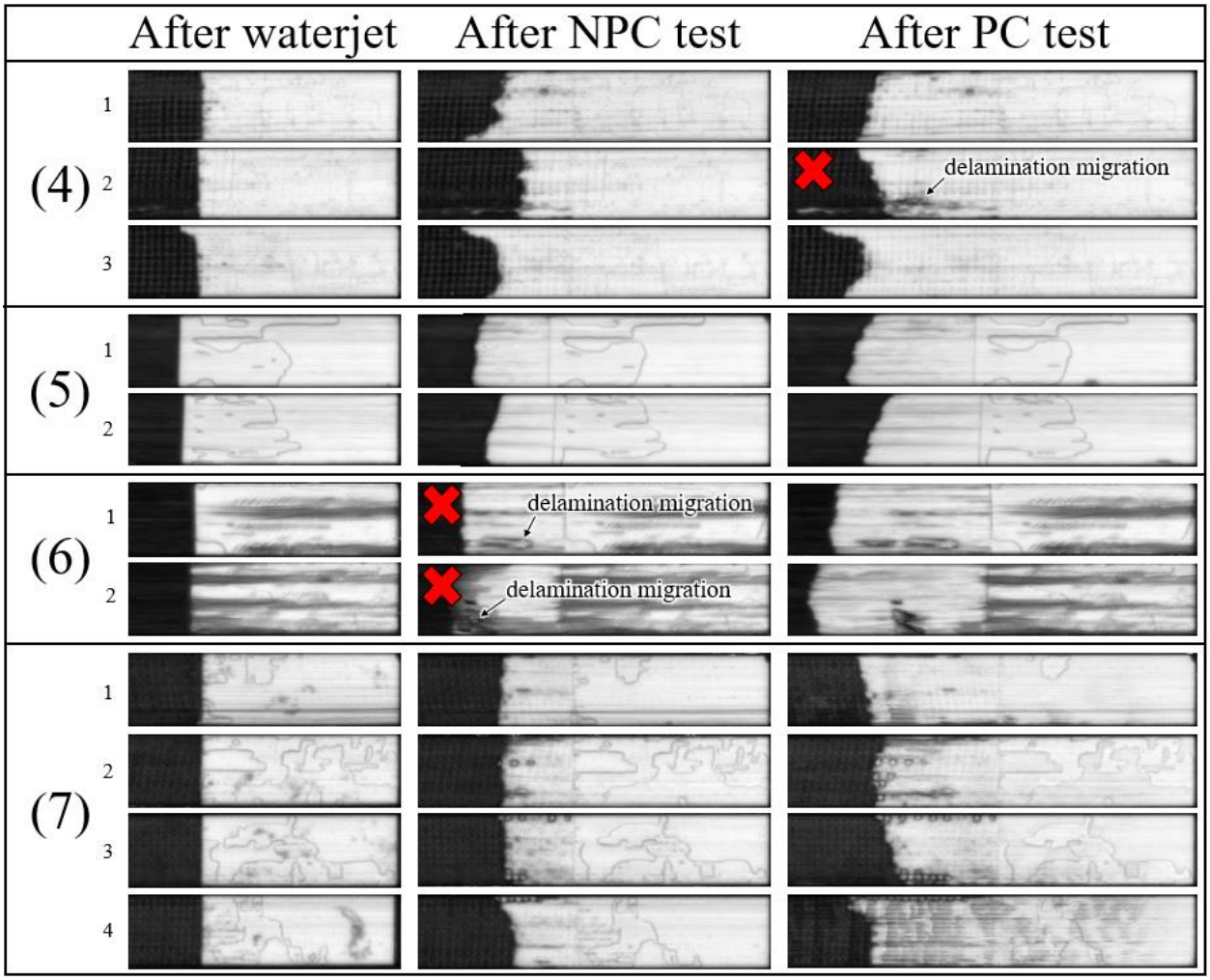

Figure 16. UT scans throughout the specimen testing process that resulted in valid test data from configurations 4-7.

4.0 CONCLUSIONS

The risk of undetectable weak bonds in primary aircraft structure is often mitigated by installing redundant fasteners in bonded joints at a significant cost and performance penalty. Composite laminates were successfully assembled in secondary (post-cure) joining processes without adhesives and with a low possibility for undetectable weak bonds. Stoichiometrically offset epoxy resins were used to assemble composite laminate joints with no discernable bondline in optical micrographs after reflow and mixing of resins at the interface during cure. Thorough test methods were employed to measure the mode II fracture toughness at the ER-HR interface to quantify joint performance. This technology enables fabrication of complex or large structures from simple components with a much-reduced probability of undetectable weak bonds.

Multiple process parameters influenced the fracture performance of experimental joints with offset epoxy resin. The stoichiometric offset, quantified by the *r*-value, must be sufficiently far from unity to prevent gelation during the primary cure. The *r*-values of 0.15 and 0.1 achieved good performance with the highest properties coming from 0.1. The areal weight and resin content of the ER and HR plies establish the r_m and diffusion distance required during each cure step to achieve good mixing and uniform composition in the joint. Generally, r_m values close to but less than 0.8 gave the best results while joints with r_m greater than one exhibited poor fracture performance. The higher resin content in the ER ply and resin retention after primary cure helped to maintain surface r_{IR}-value less than or equal to

0.15 and stayed sufficiently below the gel point to allow reflow and mixing during secondary cure. The primary cure cycle significantly impacted joint performance. Poor performance was observed after primary cure cycles with a hold of 1 h or more at 180 °C. Reducing the thermal budget in primary cure by reducing the cure temperature or time improved performance, but good performance was observed with a 45 min. hold at 180 °C or with lower temperature holds as suggested by the process simulations.

FTIR and ultrasonic inspection techniques enabled robust prediction of poor and good performing joints. A r_{IR}-value < 0.15 obtained from FTIR-ATR inspection of the ER surface after primary cure reliably indicated good fracture performance. Ultrasonic inspection clearly indicated disbond and void defects in laminates that exhibited poor fracture performance while good performing joints were defect free. Such techniques can be implemented in manufacturing for quality assurance of bondline performance for critical structural applications to provide a "go" or "no-go" for joint certification. For post-fabrication forensics, optical microscopy allowed observation of matrix resin discontinuities and microcracks at the ER/HR interface, while IR microscopy further enabled high-resolution visualization of complex chemistry changes across the entire thickness of the joints through conventional resin, ER, and HR regions.

4. REFERENCES

[1] Kruse T, Fuertes TAS, Koerwien T, Geistbeck M. Bonding of CFRP primary aerospace structures - boundary conditions for certification in relation with new design and technology developments. Society for the Advancement of Materials and Process Engineering. Seattle, WA2014. p. 15.

[2] Bossi R, Piehl MJ. Bonding primary aircraft structure: the issues. Manufacturing Engineering2011. p. 101-9.

[3] Bossi R, Carlsen R, Boerio FJ, Dillingham G. Composite surface preparation QA for bonding. SAMPE 2005. Long Beach, CA: Society for the Advancement of Material and Process Engineering; 2005.

[4] Piehl MJ, Bossi RH, Blohowiak KY, Dilligan MA, Grace WB. Efficient certification of bonded primary structure. Society for the Advancement of Materials and Process Engineering. Long Beach, CA2013. p. 649-58.

[5] Palmieri F, Ledesma R, Fulton T, Arthur A, Eldridge K, Thibeault S, et al. Picosecond pulsed laser ablation for the surface preparation of epoxy composites. Society for the Advancement of Materials and Process Engineering. Seattle, WA2017. p. 14.

[6] Oakley B, Bichon B, Clarkson S, Dillingham G, Hanson B, McFarland JM, et al. Determination of threshold levels of archetype contaminant compounds on composite adhereds and their quantification via FTIR and contact angle techniques. Annual Meeting of the Adhesion Society. San Antonio, TX2016. p. 3.

[7] Gardiner G. Building TRUST in bonded primary structures. Composites World: Gardener Business Media Inc.; 2015. p. 5.

[8] Hempe DW. Advisory Circular Number 20-107B. In: Administration USDoTFA, editor. Washington, DC: US Department of Transportation; 2010. p. 1-38.

[9] Raetzke K, Shaikh MQ, Faupel F, and Noeske P-LM. Shelf stability of reactive adhesive formulations: A case study for dicyandiamide-cured epoxy systems. International Journal of Adhesion and Adhesives, Volume 30, Issue 2, 2010, Pages 105-110.

[10] Zhang P, Shah SAA, Gao F, Sun H, Cui Z, Cheng J, Zhang J. Latent curing epoxy systems with reduced curing temperature and improved stability. Thermochimica Acta, Volume 676, 2019, Pages 130-138, ISSN 0040-6031, https://doi.org/10.1016/j.tca.2019.03.022.

[11] Wang J, Xu Y, Fu Y et al. Latent curing systems stabilized by reaction equilibrium in homogeneous mixtures of benzoxazine and amine. Sci Rep 6, 38584 (2016). https://doi.org/10.1038/srep38584.

[12] Palmieri FL, Wohl CJ, Connell JW, Mercado Z, and Galloway J. Latent Hardeners for the Assembly of Epoxy Composites. 2016 Meeting of the Adhesion Society, San Antonio, TX, 2/21-2/24 2016.

[13] MacAdams L, Kohli KD, Peel Ply for Surface Preparation and Bonding Method Using the Same. US Patent: 20210283891, filed: Dec 19, 2018.

[14] Palmieri FL, Hudson TB, Cano RJ, Tastepe E, Rufeisen D, Ahmed L, et al. Reliable Bonding of Composite Laminates using Reflowable Epoxy Resins. 2019 Meeting of the

Society for the Advancement of Materials and Process Engineering. Charlotte, NC: SAMPE; 2019.

[15] Palmieri FL, Hudson TB, Cano RJ, Tastepe E, Rufeisen D, Ahmed L, et al. Adhesive Joining of Composite Laminates Using Epoxy Resins with Stoichiometric Offset. Annual Meeting of the Adhesion Society. Hilton Head, SC2019.

[16] Hodd K. Epoxy Resins. In: Allen G, Bevington JC, editors. Comprehensive Polymer Science and Supplements: Pergamon; 1989. p. 667-99.

[17] International ASTM. Standard Test Method for Determination of the Mode II Interlaminar Fracture Toughness of Unidirectional Fiber-Reinforced Polymer Matrix Composites. West Conshohocken, PA: ASTM International; 2014. p. 18.

[18] O'Brien TK, Johnston WM, Toland GJ. Mode II Interlaminar Fracture Toughness and Fatigue Characterization of a Graphite Epoxy Composite Material. In: Center LR, editor. Hampton, VA: NASA; 2010.

[19] Cano RJ, Johnston NJ, Marchello J. Solution Prepregging Quality Control. 40th SAMPE Symposium and Exhibition. Anaheim, CA1995. p. 583-95.

[20] Harris CR, Millman KJ, Walt SJvd. Array programming with NumPy. Nature. 2020;585:357-62.

[21] Virtanen P, Gommers R, Oliphant TE. SciPy 1.0: fundamental algorithms for scientific computing in Python. Nature Methods. 2020;17:261-72.

[22] Hunter JD. A 2D graphics environment. Computer Science Engineering. 2007;9:90-5.

[23] Barber CB, Dobkin DP, Huhdanpaa H. The quickhull algorithm for convex hulls. ACM Transactions on Mathematical Software. 1996;22:469-83.

[24] Palmieri FL, Hudson TB, Smith AJ, Cano RJ, Lin Y, Kang JH, et al. Reduced Dependence on Redundant Fasteners in Secondary-Bonded Composite Structures Using Modified Epoxy Matrix Resins. 2020 Annual Meeting of the Adhesion Society. Charleston, SC2020.

[25] Palmieri FL, Hudson TB, Smith AJ, Cano RJ, Lin Y, Kang JH, et al. Modified Epoxy Matrix Resins for Reduced Dependence on Redundant Fasteners in Secondary-Bonded Composite Structures. 2020 Annual Meeting of the Society for the Advancement of Materials and Process Engineering. Seattle, WA: SAMPE; 2020.